Investigating Anomalous Photochemistry in the Inner Wind of IRC+10216 through Interferometric Observations of HC₃N

Mark A. Siebert[1] , Marie Van de Sande[2] , Thomas J. Millar[3] , and Anthony J. Remijan[4]
[1] Department of Astronomy, University of Virginia, Charlottesville, VA 22904, USA
[2] School of Physics and Astronomy, University of Leeds, Leeds, UK
[3] School of Mathematics and Physics, Queen's University Belfast, Belfast, UK
[4] National Radio Astronomy Observatory, Charlottesville, VA 22903, USA

Abstract

In recent years, many questions have arisen regarding the chemistry of photochemical products in the carbon-rich winds of evolved stars. To address them, it is imperative to constrain the distributions of such species through high-angular-resolution interferometric observations covering multiple rotational transitions. We used archival Atacama Large Millimeter/submillimeter Array observations to map rotational lines involving high energy levels of cyanoacetylene (HC₃N) toward the inner envelope (radius $< 8''/1000$ au) of the carbon star IRC+10216. The observed lines include the $J = 28 - 27$, $J = 30 - 29$, and $J = 38 - 37$ transitions of HC₃N in its ground vibrational state. In contrast to previous observations of linear carbon chains toward this asymptotic giant branch (AGB) star that show extended, hollow emission at $15''$–$20''$ radii (e.g., C₄H, C₆H, and HC₅N), the maps of the HC₃N lines here show compact morphologies comprising various arcs and density enhancements, with significant emission from gas clumps at an angular distance of $\sim 3''$ (350 au) from the central AGB star. We compared visibility sampled non-LTE radiative transfer models with the observed brightness distributions, and derive a fractional abundance with respect to H₂ of 10^{-8} for HC₃N at the radii probed by these lines. These results are consistent with enhanced photochemistry occurring in warm (~ 200 K) regions of the circumstellar envelope. After application of a specialized chemical model for IRC+10216, we find evidence that the enhanced HC₃N abundances in the inner wind are most likely due to a solar-type binary companion initiating photochemistry in this region.

Unified Astronomy Thesaurus concepts: Evolved stars (481); Astrochemistry (75); Carbon stars (199); Circumstellar envelopes (237); Chemical abundances (224)

1. Introduction

IRC+10216, also known as CW Leo, is a well-studied nearby ($d \sim 130$ pc; Men'shchikov et al. 2001) asymptotic giant branch (AGB) star with a chemically rich expanding circumstellar envelope (CSE). The CSE is the result of dust-driven mass loss at a rate of $\sim 2 \times 10^{-5}$ $M_\odot$ yr^{-1} (De Beck et al. 2012), and represents one of the final stages of evolution for 1–8 $M_\odot$ stars immediately preceding the transition between the AGB and the formation of a planetary nebula (PN). During this stage, depending on how much carbon has been convectively dredged up from the star's core relative to oxygen (Weiss & Ferguson 2009), AGB stars can either be M type (C/O < 1), C type (C/O > 1), or S type (C/O ∼ 1). IRC+10216 has a C/O ratio of 1.4 (Winters et al. 1994), which allows for a complex system of carbonaceous gas-phase and dust grain chemistry to occur throughout its extended envelope. To date, more than 95 unique molecules have been identified toward IRC+10216 (McGuire 2022). Due to its close proximity and history as a molecular line object, IRC+10216 forms the basis of our understanding on how carbon-rich stellar material is processed and returned to the interstellar medium by low- to intermediate-mass stars.

An important aspect of AGB evolution that has become clear with the advent of the Atacama Large Millimeter/submillimeter Array (ALMA) is the prevalence of binary companion

stars influencing mass loss and shaping circumstellar winds (Decin 2021). Companions are difficult to detect directly in these systems, due to the intrinsic luminosity of the AGB star and the high attenuation of visible light by their dusty envelopes. However, several recent studies of gas and dust kinematics have shown the perturbative effects binary companions can have on many AGB and proto-planetary nebula (PPNe) systems. Both small-scale asymmetries, such as density-enhanced clumps (e.g., Leao et al. 2006; Khouri et al. 2016; Agúndez et al. 2017), and large-scale structures, such as spirals (e.g., Mauron & Huggins 2006; Decin et al. 2015; Maercker et al. 2016; Ramstedt et al. 2017), disk geometries (e.g., Kervella et al. 2014; Homan et al. 2018, 2020; Sahai et al. 2022), and bipolar outflows (e.g., Lagadec et al. 2011; Kim et al. 2015b; Sahai et al. 2017) have been detected. In particular, the ALMA Large Program ATOMIUM (2018.1.000659.L; PI: Decin) has shown the widespread nature of these structures through a survey of numerous AGB outflows (Decin et al. 2020). It is now thought that the influence from stellar and planetary companions is closely related to the stark morphological changes in circumstellar material during the transition between the AGB and PN stages of evolution (Sahai et al. 2007). IRC+10216 shows signs of binary influence, based on the interspaced shells in its extended envelope (Cernicharo et al. 2015; Guelin et al. 2018), spiral structure in its inner layers (Decin et al. 2015), as well as the detection of a tentative compact source $0''.5$ from the star via archival Hubble Space Telescope (HST) monitoring by Kim et al. (2015a, 2021).

While their physical effects have been studied in detail, the chemical impact of companion stars embedded in CSEs and PPNe has not yet been observationally tested. The typical framework for how gas-phase chemistry proceeds in CSEs assumes precursor molecules (e.g., CO, HCN, and SiO) form out of a combination of equilibrium and shock-induced chemistry in the high-temperature regions near the stellar photosphere (Cherchneff 2012; Agúndez et al. 2020). Once they reach the outer regions of the envelope where the density of attenuating dust grains is lower, UV photons from the interstellar radiation field (ISRF) initiate a kinetically driven photochemistry to form a variety of exotic product molecules (e.g., HC_7N, SiN, and MgNC; Ziurys 2006; Li et al. 2016; Millar 2020). While this scheme is consistent with the measured abundances of many molecules, recent studies of IRC+10216 have revealed that this picture may be much more complicated than previously thought. Agundez et al. (2015) and Quintana-Lacaci et al. (2017) discovered that CH_3CN and NaCN are present in the inner envelope ($<5''$). This was an unexpected result as the proposed formation routes of both these molecules require photochemistry, which typically takes hold further out ($10''$–$25''$) in the CSE (Dinh-V-Trung & Lim 2008). Similar results were also found for the product molecules water (H_2O) and diacetylene (C_4H_2) (Agundez et al. 2010; Fonfria et al. 2018).

One molecule that is central to photochemistry in CSE environments is cyanoacetylene (HC_3N). In the gas phase, this species is formed primarily through the reaction between acetylene (C_2H_2) and the cyanide radical (CN), the latter of which is only available as a reactant when the flux of UV photons is large enough to efficiently dissociate the precursor molecule HCN (Agúndez et al. 2017). Because C_2H_2 is an abundant precursor molecule and one of the main carriers of carbon in C-rich CSEs (Santoro et al. 2020), HC_3N is one of the first product molecules to form out of UV-driven chemistry, making it useful in probing the photoprocessing of gas-phase material in these objects.

HC_3N and longer cyanopolyynes in the envelope of IRC+10216 were studied with the Very Large Array (VLA) by Dinh-V-Trung & Lim (2008) and subsequently with ALMA by Agúndez et al. (2017), where it was seen between $10''$ and $20''$ (1300–2600 au). This is where the HC_3N abundance is expected to peak based on photochemical models of this CSE; however, these observations targeted low-lying rotational transitions (including states up to $J = 12$ and $E_{up} = 34$ K), which naturally trace lower-temperature regions. In order to gain a more complete view of this molecule in the envelope of IRC+10216, and to better understand the onset of photochemistry in these environments, it is important to spatially constrain higher-energy transitions of HC_3N that could be discernible in the warmer regions where CH_3CN and NaCN were observed.

To this end, we present an archival study of IRC+10216 with the goal of characterizing HC_3N in the inner (arcsecond-scale) layers of its envelope. We utilize observations from three separate ALMA projects to analyze the spectra and spatial distributions of the $J = 28 - 27$, $J = 30 - 29$, and $J = 38 - 37$ lines of HC_3N toward IRC+10216. Using maps of these lines at the systemic velocity combined with radiative transfer models, we quantify the abundance of HC_3N in the inner regions of IRC+10216 and discuss how they affect our understanding of photochemical processing in this CSE. In Section 2 we describe the observations and reduction procedure, in Section 3.2 we present emission maps, in Section 3.3 we use non-LTE radiative transfer models to derive the abundance profile of HC_3N, and in Section 4 we utilize a specialized photochemistry model to compare our observations with kinetic theory and test the hypothesis that molecules surrounding IRC+10216 are affected by a binary stellar companion embedded in the inner envelope.

2. Observations and Reduction

We utilize observations from three publicly available archival ALMA projects to map warm HC_3N emission toward IRC+10216. Figure 1 demonstrates the different antenna configurations and coverage of the u–v plane for the data sets, while Table 1 summarizes these different observations and the target HC_3N transitions for this work. Project 2019.1.00507.S provides several spectral scans of IRC+10216 at Band 6 between 250 and 270 GHz using both the main 12 m array and the 7 m Atacama Compact Array (ACA). These observations were used by He et al. (2019) to study the time-variability of millimeter lines toward IRC+10216, and cover the $J = 28 - 27$ transition of HC_3N. In order to recover flux from as many spatial scales as possible, we combined visibility measurements from four separate array configurations included in this project, including two 12 m executions with baseline lengths ranging from 15 to 1230 m and two ACA measurements covering baselines between 9 and 50 m (see Figure 1). Data combination was performed with antenna-specific weighting, and the resulting images have a maximum recoverable scale of $30''$.

Project 2011.0.00229.S provides a Cycle 0 spectral line survey of IRC+10216 covering most of Band 6 using the 12 m array, allowing emission from the $J = 30 - 29$ transition to be mapped as well; however, only 18 antennas were available at this time, as opposed to the 42 that were used for the later data sets. These data cover baselines ranging from 27 to 402 m with a maximum recoverable scale of $\sim 1''$.

Project 2016.1.00251.S provides a Band 7 observation between 330 and 346 GHz using the 12 m array. This ALMA configuration includes baselines between 15 and 314 m, and offers a maximum recoverable scale of $8''$. These data were used to map the $J = 38 - 37$ line of HC_3N in addition to the $J = 3 - 2$ line of ^{13}CO at $\nu_{rest} = 330{,}588.0$ MHz. The ^{13}CO observations are useful in qualitatively characterizing the overall envelope density structure.

As Figure 1 demonstrates, the ALMA Projects we utilize have very different antenna setups and consequently disparate spatial frequencies sampled. Due to these differences between instrument configurations and the nonuniqueness of the image reconstruction process, care must be taken when directly comparing brightness distributions between data sets. All observations were pointed near the continuum peak of IRC+10216 at $\alpha_{J2000} = 09^h 47^m 57{.}^s458$, $\delta_{J2000} = +13°16'43{.}''90$, despite having slightly different phase centers between projects. Errors in pointing were estimated to be 30 mas for the $J = 28 - 27$ observations, and 40 mas for the $J = 30 - 29$ and $J = 38 - 37$ observations.[5]

All data were calibrated using the standard calibration pipeline of the Common Astronomy Software Application (CASA; McMullin et al. 2007). Visibilities from the Band 6

---

[5] Referencing Section 10.5.2 of the ALMA Technical Handbook (Cortes et al. 2020).
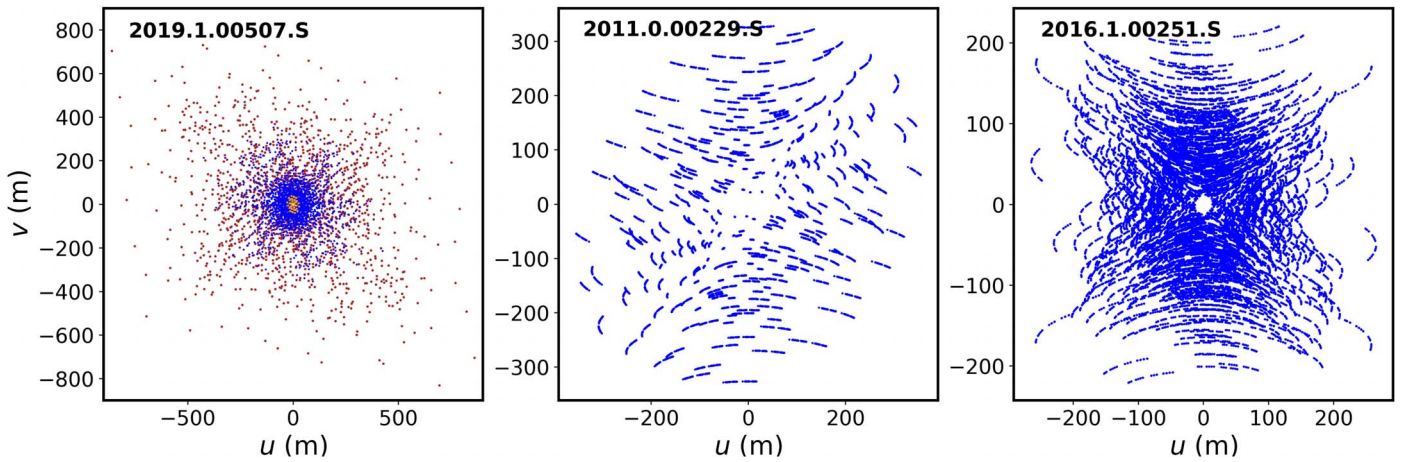
Figure 1. Coverage of the *u–v* plane offered by the three ALMA projects utilized in this work. Baselines from compact 12 m configurations are shown in blue, those from extended 12 m configurations are shown in brown, and 7 m ACA baselines are shown in orange. Observations from left to right were used to image the $J = 28 - 27$, $J = 30 - 29$, and $J = 38 - 37$ transitions of HC$_3$N, respectively.

data sets were resampled to a spectral resolution of $1.7 \, \text{km s}^{-1}$ to match the correlator configuration in the Band 7 project. Continuum subtraction was done in visibility space using line-free channels present in each spectral window containing HC$_3$N. Then, imaging was performed with the TCLEAN CASA task, using Briggs weighting with a 0.5 robustness parameter for the $J = 28 - 27$ and $J = 38 - 37$ lines, and natural weighting for the $J = 30 - 29$ line due to its lower signal-to-noise ratio. Iterative masking was done with user-defined regions to optimize the deconvolution process. In the case of the $J = 28 - 27$ line, multiscale cleaning was applied to account for the multiple combined array configurations (Cornwell 2008). All rest frequencies were obtained from the Cologne Database of Molecular Spectroscopy (CDMS; Muller et al. 2005), and shifted to the systemic velocity of IRC +10216, $V_{\text{sys}} = -26.5 \, \text{km s}^{-1}$ (Cernicharo et al. 2000).

3. Results

3.1. Spectra, Interloping Lines, and Flux Recovery

Integrated spectra from each synthesized image cube were obtained using a 30″ circular aperture centered on IRC+10216. These spectra are shown in Figures 2(a)–(c). In these, we see emission in the characteristic "double-horned" line profile centered on the systemic velocity of $-26.5 \, \text{km s}^{-1}$, as well as some contributions from interloping lines. For the $J = 28 - 27$ line of HC$_3$N, a very close blend is seen with the $J(K_a, K_c) = 4(0, 4) - 3(0, 3)$ transition of methanimine (CH$_2$NH) at $\nu_{\text{rest}} = 254,685.1 \, \text{MHz}$. This line appears 14 MHz ($17 \, \text{km s}^{-1}$) from the central frequency of HC$_3$N. In the spectrum (Figure 2(a)), a double horn profile of CH$_2$NH can be seen with the blueshifted peak falling very close to the central channel of HC$_3$N. This blend was also detected by Tenenbaum et al. (2010). Since the aim of this study is to characterize the radial abundance using channel maps made at the systemic velocity, we must take care to make sure we do not attribute blueshifted CH$_2$NH emission to HC$_3$N. However, considering the geometry of spherical outflows and empirical evidence from previous ALMA studies of AGB stars (e.g., channel maps in Decin et al. 2018 and Brunner et al. 2018), we expect that the contamination from the highest-velocity emission is limited only to the smallest spatial scales and appears very close to the position of IRC+10216.

In the case of the $J = 38 - 37$ line of HC$_3$N (Figure 2(c)), there is a slight blend with the $J(K_a, K_c) = 15(14, 1) - 15(14, 0)$ transition of SiC$_2$ at $\nu_{\text{rest}} = 345,575.2 \, \text{MHz}$. This lies 34 MHz ($29 \, \text{km s}^{-1}$) away from the central frequency of our target HC$_3$N line, so with a half-line width of $14.5 \, \text{km s}^{-1}$, only the most redshifted channels of the image cube are contaminated by emission from SiC$_2$.

The $J = 28 - 27$ and $J = 30 - 29$ lines of HC$_3$N were also observed in the single-dish line surveys of He et al. (2008) and Tenenbaum et al. (2010), both using the Arizona Radio Observatory 10 m Submillimeter Telescope (SMT). These works provide useful data points that allow us to characterize the amount of spatial filtering in our interferometric measurements of the same lines. Both He et al. (2008) and Tenenbaum et al. (2010) detected the $J = 28 - 27$ line of HC$_3$N with a peak brightness temperature $T_R = 130$ mK. Considering that the SMT has a half-power beam width of 30″ at 254.7 GHz, we can compare this directly with the spectrum in Figure 2(a), which peaks at 120 mK. In contrast, the $J = 30 - 29$ line shown in Figure 2(b) was detected in Tenenbaum et al. (2010) with a peak temperature of $T_R = 90$ mK, while we instead obtain a value of 10 mK. It is clear that the observations from Project 2019.1.00507.S, which comprise both ACA and multiple 12 m executions spanning a large range of baselines, are able to recover more than 90% of the HC$_3$N ($J = 28 - 27$) emission. However, the Cycle 0 observations of the $J = 30 - 29$ line exhibit a large amount of spatial filtering due to the lower number of antennas and poorer *uv* coverage. Unfortunately, there exist no published single-dish measurements for the $J = 38 - 37$ transition of HC$_3$N toward IRC+10216, but we still take steps to account for the flux loss of these measurements, described in Section 3.3.

3.2. Emission Maps

Reconstructed maps of the three studied HC$_3$N lines are shown in Figure 3. All images were made at the systemic velocity of IRC+10216 ($V_{\text{sys}} = -26.5 \, \text{km s}^{-1}$). These maps show morphologies centered on the position of the AGB star with emission primarily within a radius of 5″. The distribution of the $J = 28 - 27$ line includes an extended component out to 3″ surrounded by several asymmetric arcs and clumps (Figure 3(a)). Due to the higher temperatures probed by this

Table 1
Summary and Characteristics of the ALMA Data Utilized in This Work

ALMA Project Code	Obs. Date(s)	Array(s)	Synthesized Beam $(\theta_{maj} \times \theta_{min})$	HC$_3$N Line $(J' \to J'')$	Rest Frequency (MHz)	E_{up} (K)	Image rms (mJy beam^{-1})
2019.1.00507.S	2019 Nov–2020 Mar	12m + 7 m	$0\rlap{.}{''}480 \times 0\rlap{.}{''}449$	$28 \to 27$	254,699.5	177	1.8
2011.0.00229.S	2012 Apr	12 m	$0\rlap{.}{''}725 \times 0\rlap{.}{''}520$	$30 \to 29$	272,884.7	203	7.2
2016.1.00251.S	2018 May	12 m	$0\rlap{.}{''}848 \times 0\rlap{.}{''}761$	$38 \to 37$	345,609.0	324	1.9

Note. Observations from ALMA Project 2019.1.00507.S include two 12 m configurations and two from the 7 m ACA. Transition frequencies and upper-state energies were obtained from the Cologne Database of Molecular Spectroscopy (CDMS; Muller et al. 2005). Reported rms values were measured from an emission-free channel of the final reconstructed image cube.

transition, the majority of its emission traces regions entirely separated from that observed in the lower-excitation lines mapped by Agúndez et al. (2017) and Dinh-V-Trung & Lim (2008) ($J = 10 - 9$ and $J = 5 - 4$; which peak at radius 14″), with the notable exception of a region to the SW at a radius of 10″. In the central component (within 3″), the average brightness of the $J = 28 - 27$ line is a 10 mJy beam^{-1}, with notable bright clumps to the N and SW. Although a central point source is seen at the position of the carbon star, we expect that this is contributed from the most blueshifted channel of the weak interloping line of CH$_2$NH (see Section 3.1 and Figure 2), since this peak is notably absent from the unblended image in Figure 3(c).

The $J = 38 - 37$ line (Figure 3(c)) also shows bright, spatially resolved emission that is entirely distinct from the maps of HC$_3$N in Agúndez et al. (2017). In contrast to $J = 28 - 27$, the distribution of this line is entirely concentrated within a radius of 4″ and shows no central peak on the position of IRC+10216, since there is no contaminating emission present in this channel. The imaged line is again not azimuthally symmetric, and traces the same bright clumps and arcs seen in the $J = 28 - 27$ line. It reaches a peak brightness of 122 ± 1.9 mJy beam^{-1} in the SW clump at 2″. The more compact morphology can be qualitatively explained by the higher upper-state energy (323 K) and larger (by a factor of 3) Einstein A_{ij} coefficient of this transition relative to the $J = 28 - 27$ line.

Finally, Figure 3(b) shows the $J = 30 - 29$ line, which also appears toward the same bright clump ~2″ to the SW. However, due to the sensitivity of these data, very little additional emission is seen from this transition. If this line has a similar extended component, as seen in $J = 28 - 27$, we would expect most of this flux to be resolved out by the interferometer given its maximum recoverable scale. However, if the $J = 30 - 29$ line had a compact, point-like component at the position of IRC+10216 with a similar peak brightness to the SW clump (as is the case with $J = 28 - 27$), we would expect to detect that even at the limited sensitivity of these data. Due to the similar excitation conditions of the $J = 30 - 29$ and $J = 28 - 27$ lines, we take this as further evidence of the central peak in Figure 3(a) being contributed by CH$_2$NH, and not HC$_3$N. Nevertheless, because of the observational limitations of this ALMA project (2011.0.00229.S), we do not include this line in our radiative transfer analysis.

Figure 4 shows the observed HC$_3$N lines as contours overlaid on the image of ^{13}CO $J = 3 - 2$ at $\nu_{rest} = 330{,}587.97$ MHz created from the Band 7 ALMA observations. Using a CO abundance of 6×10^{-4} (Agúndez et al. 2012; De Beck et al. 2012) and a ^{12}C/^{13}C ratio of 48 (Knapp & Chang 1985), we adopt a constant ^{13}CO abundance

of 1.3×10^{-5} with respect to H$_2$ throughout the regions of IRC +10216 we are investigating. Therefore, it is a useful indicator of the density structure. Keeping in mind the spatial filtering effects due to the lack of very short antenna spacings in these data, we see that the structures traced by HC$_3$N are spatially coincident with density enhancements resulting from nonisotropic mass loss. The clump SW of IRC+10216 that is seen in all three observed HC$_3$N lines is also apparent here as the brightest area of ^{13}CO emission away from the central point source (see Figure 4). Between the bright arcs we see several areas of negative flux, which are image artifacts resulting from resolved-out emission and not indicative of actual absorption. When compared with images in Agundez et al. (2015), we find that both HC$_3$N and ^{13}CO trace similar compact structures to CH$_3$CN ($J_K = 14_3 - 13_3$), including the SW clump.

3.3. Radiative Transfer Modeling

In order to draw conclusions regarding the abundance of HC$_3$N, we must first consider the excitation physics of this molecule in the inner envelope of IRC+10216. In many cases, LTE is a good approximation for chemical studies of CSEs due to their high central densities. However, the rotational transitions observed here have comparatively large Einstein A_{ij} coefficients ($10^{-2.9}$–$10^{-2.5}$ s^{-1}), so it is possible that they are subthermally excited even at arcsecond scales. In Figure 5, we show the predicted excitation temperatures of the three HC$_3$N transitions as a function of gas density for two different kinetic temperatures, generated using the RADEX radiative transfer software (van der Tak et al. 2007). Using the one-dimensional (1D) density law from Equation (1) in Agúndez et al. (2012) along with a mass-loss rate of 2.7×10^{-5} $M_\odot$ yr^{-1} (Guelin et al. 2018), we also show the expected average gas densities at the radii where most of the emission is seen (between 1″ and 5″). From this, it is clear that LTE could only be assumed if the densities were higher than 10^8 cm^{-3}, and the observed gas density is below the critical densities of all three HC$_3$N transitions in the mapped regions. Furthermore, pumping to vibrational states via thermal IR photons from dust grains has been shown to be an important excitation mechanism in the envelope of IRC+10216 (Deguchi & Uyemura 1984; Keady & Ridgway 1993; Fonfria et al. 2008; Cernicharo et al. 2014; Agúndez et al. 2017), so non-LTE calculations are necessary to take all of these factors into account.

Therefore, we adopt a forward-modeling approach in predicting the expected brightness distributions and determining the abundance of HC$_3$N needed to reproduce the maps in Figure 3. We utilize the LIne Modeling Engine (LIME) to simulate the level populations of HC$_3$N, solve the radiative transfer equation, and produce synthetic image cubes (Brinch
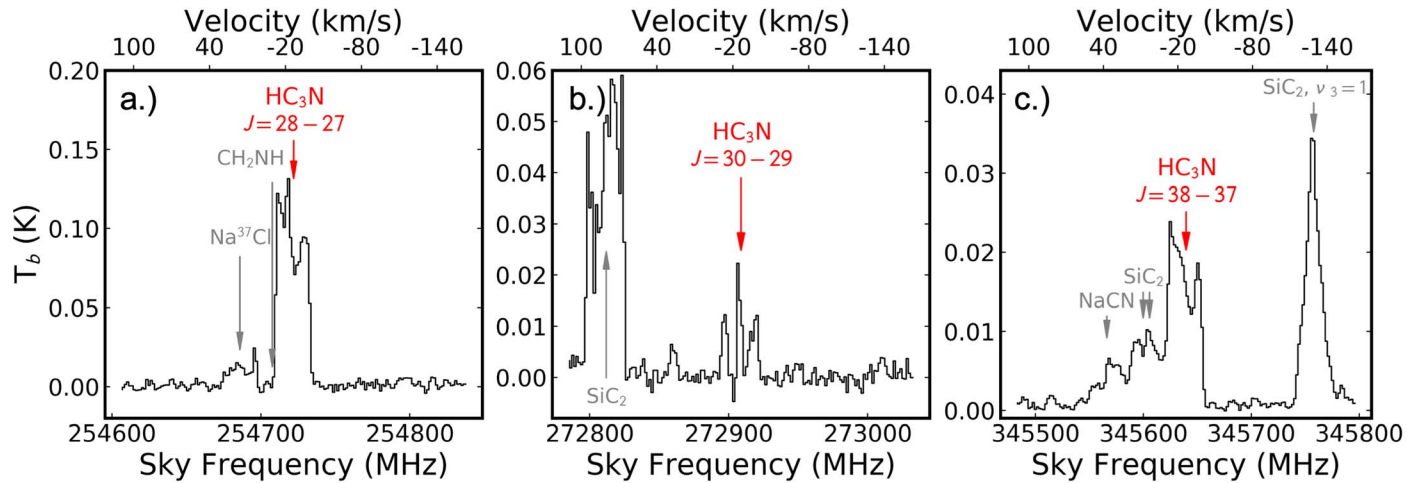
Figure 2. Spectra demonstrating the three HC$_3$N lines studied in this work (red), in addition to nearby and interloping molecular lines (gray). Spectra were created from image cubes using a 30″ aperture centered on the position of IRC+10216. The lower x-axes denote sky frequencies, while the upper axes show velocity using the rest frequency of the respective HC$_3$N transition. All transitions are from the ground vibrational state unless indicated otherwise.

& Hogerheijde 2010). LIME uses density-weighted grid points distributed in a computational space using Delaunay triangulation. Populations are solved based on the local conditions of the corresponding Voronoi cells, as well as the incident radiation from adjacent cells. For all our calculations, we use 50,000 grid points in a computational volume with radius 130,000 au (1000″). Though LIME performs these calculations in three-dimensional (3D) space, we use a 1D approximation for the physical structure of IRC+10216, since the 3D asymmetries apparent in Figures 3 and 4 are not presently constrained in their local physical conditions and require hydrodynamical simulations that are outside the scope of this work. In general, we adopt the same model for the CSE of IRC+10216 as Agúndez et al. (2012). This includes the stellar parameters, velocity structure, gas and dust temperature profiles, and density gradient. The only difference in our physical model is the use of a slightly larger mass-loss rate of 2.7×10^{-5} $M_\odot$ yr^{-1}, as this value was measured by Guelin et al. (2018) specifically using CO emission at radii within 15″, meaning it is better suited for this study of warm HC$_3$N emission. The gas density in the extended envelope is given by

$$n(r) = \frac{\dot{M}}{4\pi r^2 v_\infty m_g}, \qquad (1)$$

where $\dot{M}$ is the mass-loss rate, r is the radius, v_∞ is the expansion velocity, and m_g is the average gas particle mass taken as 2.3 amu considering H$_2$, He, and CO (Agúndez et al. 2012). As such, a change in $\dot{M}$ has a significant effect on molecular volume densities and corresponding line intensities. This should be kept in mind when comparing our results with previous chemical studies of IRC+10216 that use the more typical value of 2.0×10^{-5} $M_\odot$ yr^{-1} (Agundez et al. 2015; Agúndez et al. 2017; Quintana-Lacaci et al. 2017).

For spectroscopic data, the Leiden Atomic and Molecular Database provides collisional rates of ^{13}CO and HC$_3$N with ortho- and para-H$_2$ (van der Tak et al. 2020). The ortho/para-H$_2$ ratio is assumed to be 3 at all locations in the envelope. For HC$_3$N, the collisional rates measured by Faure et al. (2016) only go up to the $J = 37$ rotational state, so we extrapolated these to the $J = 45$ level and use line strengths from CDMS for the added radiative transitions (Muller et al.

2005). The $J = 45$ level was chosen to account for population in rotational states above $J = 38$ while keeping the computational load low. We note that the choice of this maximum level had little effect on the predictions, as we found that running the model with maximum $J = 40$ and $J = 50$ yielded nearly identical results.

In addition, we included the first excited states of the ν_5 and ν_6 vibrational modes at 663 and 499 cm^{-1} (Jolly et al. 2007) using radiative rates from the HITRAN database (Gordon et al. 2022). The effect of including these states is similar to the result of Massalkhi et al. (2019), where emission is shifted to larger radii as cooler molecules could be pumped to higher J values by first being radiatively excited into these vibrational states then subsequently deexciting through the P-branch ($\Delta J = +1$) (Costagliola & Aalto 2010). Collisional transitions within vibrational states were not considered, as the timescales of vibrational deexcitation ($\sim 10^{-4}$ s) are several orders of magnitude shorter than the expected collisional excitation rates ($\sim 10^4$ s). To model thermal emission from dust grains, we use the opacity law of Ossenkopf & Henning (1994).

After obtaining ray-traced simulated image cubes from LIME, we test two separate post-processing methods before comparing with observations. The first involves a simple image plane continuum subtraction followed by convolution of the channel maps with the synthesized beams in Figure 3. For the second method, we utilize the Python module vis_sample[6] to simulate the incomplete sampling of sky brightnesses using input uv grid points directly from the observation sets. The results are simulated visibilities that were then continuum subtracted and imaged in the same manner as their respective observations (described in Section 2). The estimated flux error in the simulated image is 5%, based on the converged signal-to-noise of the individual grid points. Because the input model is spherically symmetric, we take the azimuthal average of the LIME-generated channel map at the systemic velocity of IRC +10216 to compare the modeled emission with ALMA images.

The result of both methods when applied to the $J = 3 - 2$ line of ^{13}CO, for which the abundance is known a priori, is

---

[6] vis_sample is publicly available under the MIT license at https://github.com/AstroChem/vis_sample and described in further detail in Loomis et al. (2018).
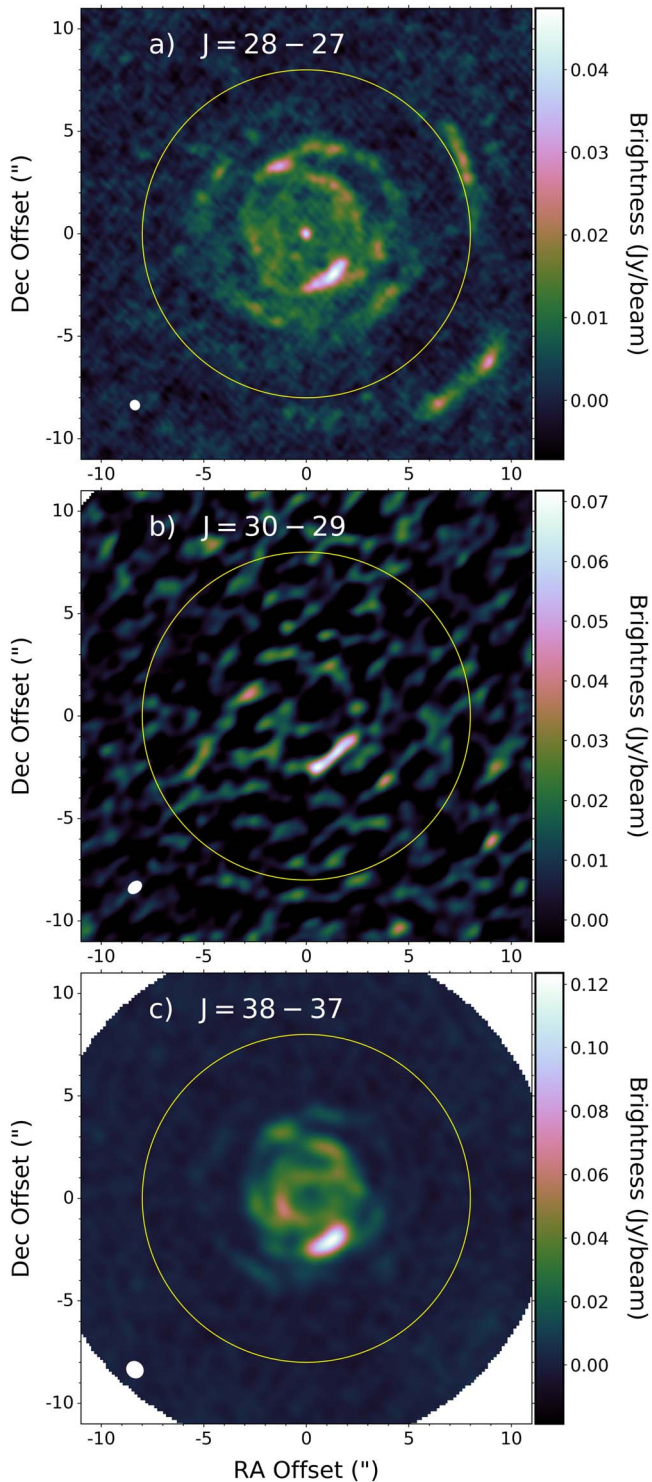
Figure 3. ALMA emission maps of three HC$_3$N lines toward IRC+10216. Images were created at a systemic velocity of -26.5 km s^{-1} with a channel width of 1.69 km s^{-1}. IRC+10216 is located at the center of the maps at $\alpha_{J2000} = 09^h47^m57^s458$, $\delta_{J2000} = +13°16'43''90$, and a reference circle with diameter 15'' is shown in yellow. Because data from separate observation sets are used, the beam sizes and absolute brightness scales are different for each panel. The shapes of the synthesized beams are shown in the bottom-left corner, with sizes 0''48 × 0''45, 0''73 × 0''52, and 0''85 × 0''76 from top to bottom.

shown in Figure 6(a). The convolved LIME model of this line overpredicts the brightness, especially in the extended layers of IRC+10216. In contrast, the visibility-sampled and reconstructed image reproduces the peak brightness to within 5%, and predicts the much lower average brightness of this line due to spatial filtering. From this it is clear that the latter method better accounts for the lack of data from short baselines and the resulting flux loss at large spatial scales, so we employ the visibility-sampling routine for the case of HC$_3$N as well.

3.3.1. Results for HC$_3$N

We use the above forward-modeling routine to simulate the $J = 28 - 27$ and $J = 38 - 37$ lines of HC$_3$N, now varying the abundance to reproduce the observed radial brightness distribution. Primarily, we modify it at radii less than 4'', since this is where we see the bulk of emission (shaded regions in Figure 7); however, we also adjust the peak abundance to reflect the observed lack of emission at radii larger than 8''. We start with a function similar to the modeled result in Agúndez et al. (2017), with a peak abundance of 1×10^{-6} at $r = 3 \times 10^{16}$ cm that steadily decreases inwards, and drops off steeply outwards. We then adjust the magnitude shape to match the distribution and intensity, by eye, of azimuthally averaged emission for both HC$_3$N lines.

The resulting simulated intensity profiles are shown in Figures 6(b) and (c). The corresponding best-fit abundance profile is shown in Figure 7(a), and the volume density is shown in Figure 7(b). The resulting modeled intensity curves are in good agreement with the observed azimuthal averages at the radii where we see the bulk of HC$_3$N emission. There is a slight disagreement in the regions between 8'' and 14'' where the average predicted $J = 28 - 27$ emission increases 2 mJy beam^{-1}; however, this is very close to the rms of the observations, so it is not expected that we would detect consistent emission at this level. We do detect some clumps with a peak abundance of 25 mJy beam^{-1} in these regions, as seen outside the yellow reference circle to the SW and NW in Figure 3(a), but no extended component is found.

In the inner layers where the HC$_3$N emission is primarily seen, an average abundance of $\sim 10^{-8}$ is needed, and it must be decreasing inward to avoid centrally peaked channel maps. In typical fashion for characterizing the radial abundance distributions of molecules forming in outer regions of CSEs (e.g., Agundez et al. 2015), we parameterize this with a Gaussian offset in log radius:

$$f(r) = f(r_p)\exp\left(-\left(\frac{\log r - \log r_p}{\Delta \log r}\right)^2\right), \qquad (2)$$

where f is the fractional abundance with respect to H$_2$, r_p is the peak radius, and $\Delta \log r$ adjusts the width of the feature. For the retrieved profile, we obtain $f(r_p) = 2.5 \times 10^{-8}$, $r_p = 2 \times 10^{16}$ cm, and $\Delta \log r = 1.65$. This is the main function we use to describe the HC$_3$N abundance in the regions of IRC+10216 probed by our observations, and an additional narrow component peaking at $r = 3 \times 10^{16}$ cm with $f = 7 \times 10^{-7}$ is included to reflect radii larger than 10^{16} cm. This is smaller than the peak derived in Agúndez et al. (2017) by a factor of 1.4, but this inconsistency is expected since a smaller mass-loss rate is used in that work. The retrieved abundance profile is shown in Figure 7(a) along with the results of a chemical model for IRC+10216, which is described in Section 4.1.
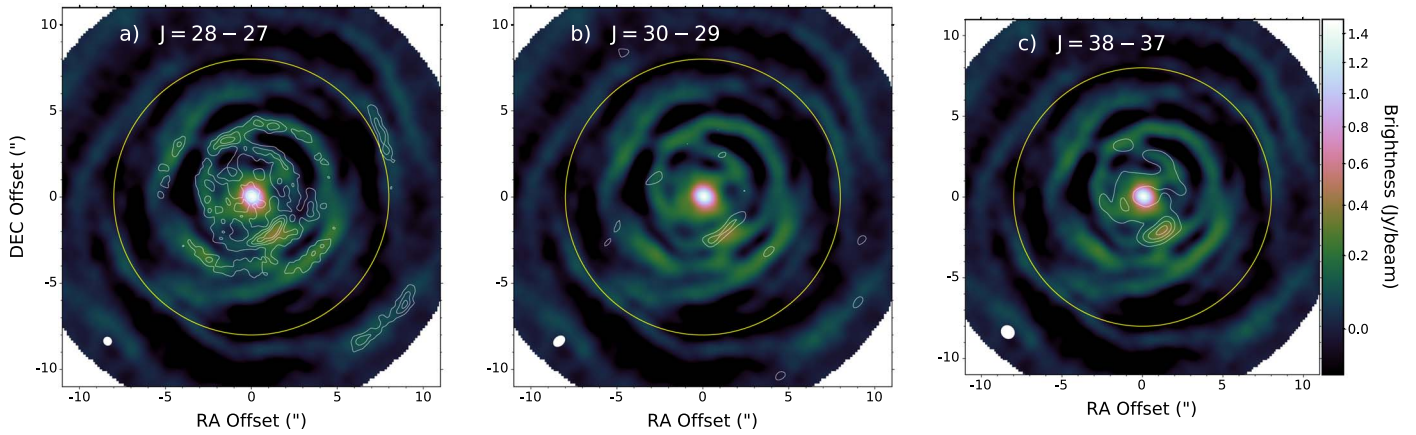
Figure 4. Contour maps of HC_3N $J = 28 - 27$, $J = 30 - 29$, and $J = 38 - 37$ (white) overlaid on the image of ^{13}CO $J = 3 - 2$ toward IRC+10216. All components are again taken at the systemic velocity and centered at the position of IRC+10216 $\alpha_{J2000}=09^h47^m57^s.458$, $\delta_{J2000} = +13°16'43''.90$, and the yellow circle denotes a radius of $7''.5$. Contour levels for each line are shown at 3, 6, 9, and 12 times the rms.
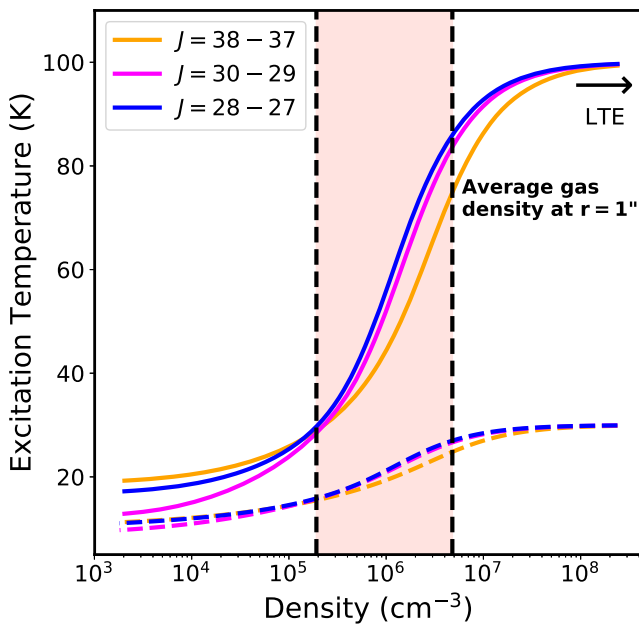
Figure 5. RADEX models of the three observed transitions of HC_3N run for a range of densities at $T_k = 30$ K (dashed lines) and $T_k = 100$ K (solid lines). The shaded region denotes the average gas densities at radii where we observe these lines toward IRC+10216 (between $1''$ and $5''$).

4. Discussion

When compared with the results of our own chemical model as well as the abundances in Agúndez et al. (2017), the measured HC_3N abundances demonstrated in Figure 7 is about 1 order of magnitude larger than predictions of kinetic chemistry at radii less than 10^{16} cm. The disparity with Agúndez et al. (2017) is actually greater than that since a lower mass-loss rate was adopted in that work, which will naturally yield higher abundances necessary to reproduce a given observation.

One factor that could potentially affect abundance calculations in the envelope of IRC+10216 is the variability of rotational molecular lines with stellar phase. Pardo et al. (2018) observed periodicity in 3 mm radical, polyyne, and cyanopolyyne species (including HC_3N) that can be either in or out of phase with the ~640 days periodicity of the AGB star as seen in the IR. He et al. (2017) observed the same behavior in

higher-frequency lines, including the $J = 28 - 27$ blend mapped in this work. We do not expect this to have a dramatic effect on our results, mainly because the amplitude of these oscillations are relatively small (ranging from 8% to 15% of the average integrated line flux), but also because the combined data we use for the $J = 28 - 27$ line were taken, and thereby averaged, over the course of 5 months, almost a quarter of the full period. Nevertheless, if we extrapolate the light curve from He et al. (2017) for the periodicity to the dates of the ALMA observations (2019 November–2020 March), we find that the map in Figure 3(a) represents phases near an expected *minimum* of this line. The $J = 38 - 37$ image was made from a single observation in 2018 May, meaning it would instead be expected to near the average brightness if it follows the same function. Once again, however, this is likely a very minor effect on the retrieved abundances since the amplitude of variation is small, especially when taken in comparison to the brightness variation from the asymmetric 3D nature of the outflow (illustrated by the shaded curves in Figure 6), which is the primary source of uncertainty in our analysis.

With this in mind, our results indicate that some process is enhancing the photochemical production of HC_3N in the envelope of IRC+10216. Therefore, our observations of HC_3N in the inner layers of IRC+10216 follow a pattern of previous results for product molecules in this envelope, namely the studies of CH_3CN, NaCN, H_2O, and C_4H_2 (Agúndez et al. 2010, 2015; Quintana-Lacaci et al. 2017; Fonfria et al. 2018). The former is driven by the radiative association of photoionized CH_3^+ with HCN, while NaCN is thought to form via a reaction between NaCl and CN (Petrie 1996; Agundez et al. 2008). H_2O and C_4H_2 have formation routes through reactions with the photodissociation products C_2H and neutral O. HC_3N formation in the extended CSE is likewise governed by the following reactions:

$$HCN + h\nu \rightarrow CN + H, \qquad (3)$$

$$C_2H_2 + CN \rightarrow HC_3N + H. \qquad (4)$$
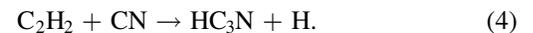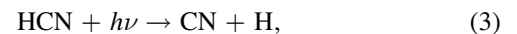
In common between all these reaction pathways is the need for a source of UV photons to provide the necessary reactants. The anomalous overabundances for all four of these species thus suggest a larger flux of UV radiation than expected in the inner envelope. Agundez et al. (2015) investigated the possibility that CH_3CN abundances result from the asymmetric clumpiness of
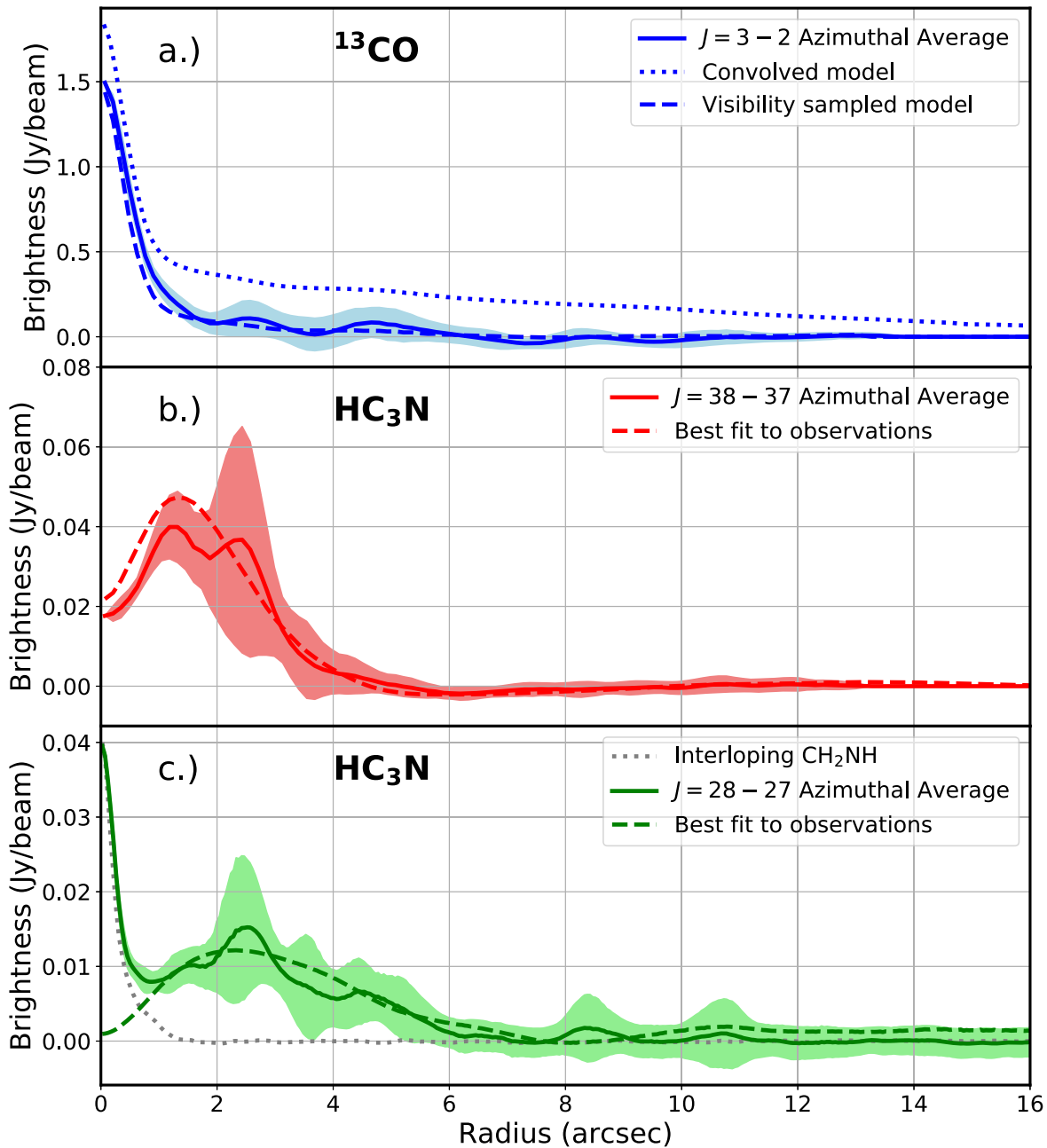
Figure 6. Observed (solid lines) and LIME-simulated (dashed lines) brightness profiles of ^{13}CO, HC$_3$N $J = 38 - 37$, and HC$_3$N $J = 28 - 27$ from top to bottom. Profiles were obtained by taking the azimuthal average of the channel map at the systemic velocity of IRC+10216 centered on the position of the AGB star. Shaded regions denote the standard deviation of the surface brightness in each radial bin. In the top panel, the profile is also shown when a convolution with the synthesized beam of observations is used instead of visibility sampling. In the bottom panel, the expected contaminating emission from CH$_2$NH is shown as well (dotted line).

the outflow allowing ionizing photons from the ISRF to penetrate farther into the outflow than the smooth spherical case; however, this was also not enough to reproduce their observations. Here, we explore an alternate scenario where the missing UV is provided internally from a binary companion star orbiting IRC+10216 at a close distance.

Evidence of such a companion existing nearby IRC+10216 has grown over recent years, primarily through spatial studies of CO and its isotopologues. Cernicharo et al. (2015) and Guelin et al. (1993) note the 16″ (~700 yr) spacing of the outermost bright gas shells, which is neither consistent with the approximate timescales of thermal pulses (~10^4 yr) nor the pulsations exhibited by AGB stars (~1 yr). These authors

suggest that the shells could instead be explained by a companion on an elliptical orbit periodically affecting the mass-loss rate of IRC+10216 during periastron. Guelin et al. (2018) found that the spacing of these shells decreases moving inwards, indicating mass transfer or additional dynamics occurring. In addition, Decin et al. (2015) detected signatures of spiral arm structure at arcsecond scales, which are consistent with a main-sequence 1 $M_{\odot}$ companion orbiting at ~20 au with an orbital period of 55 yr. Lastly, Kim et al. (2015a, 2021) detected a secondary point source of optical light about 0″.5 E of IRC+10216 using HST monitoring. Based on its spectral index, they argue that the object could be a binary companion of spectral type M1, but this result has yet to be confirmed. In
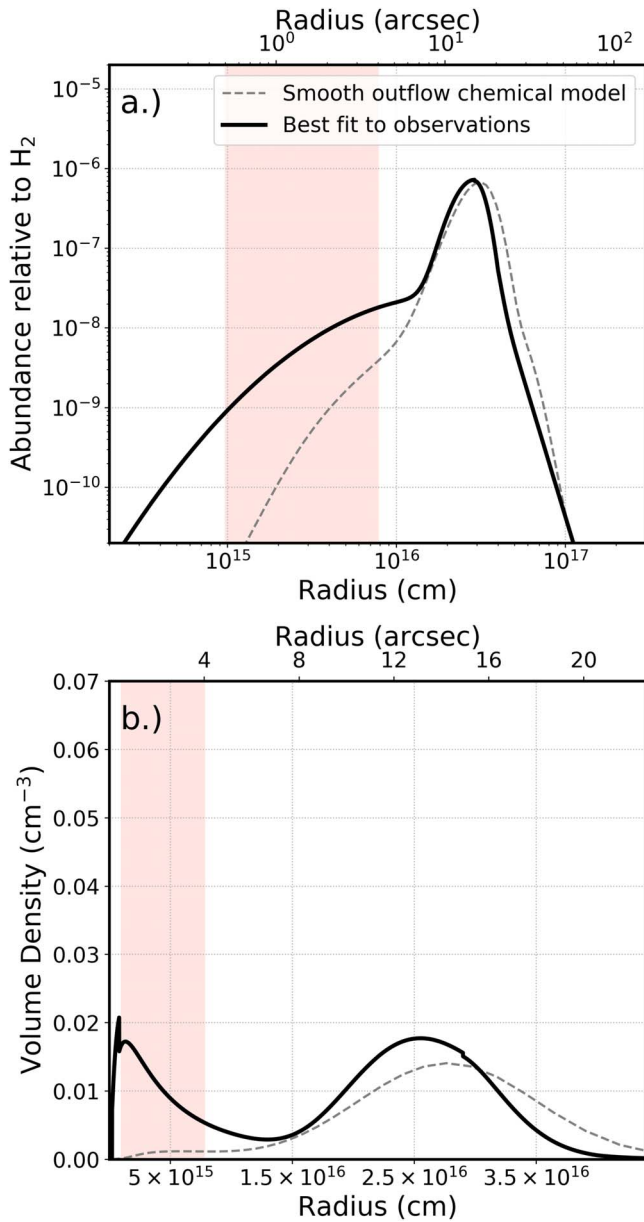
Figure 7. Radial abundance with respect to H_2 (top) and volume density (bottom) profiles of HC_3N in the envelope of IRC+10216. Solid black line represents the best-fit profile resulting from the visibility-sampled LIME radiative transfer models, while the dashed gray line is the prediction of a simple kinetic chemistry model (described in Section 4.1). The shaded red region represents the radii where the HC_3N abundance is best sampled by the observations.

the proposed scenarios of Kim et al. (2015a) and Decin et al. (2015), the binary separation is less than the minimum beam size of our observations, and in the case of Guelin et al. (2018) the proposed separation would be $\sim 1''$. So, we expect the region of the possible companion to be unresolved, or at most very weakly resolved, from the central AGB star in our observations.

While the exact nature of the orbital system IRC+10216 appears to be a part of is still not well-characterized due to uncertainties in the above works, a binary scenario seems very likely. Although IRC+10216 itself is likely far too red to produce enough UV flux to drive photochemistry in the inner envelope, a companion with a higher surface temperature could

accomplish this. To test this scheme in comparison to our measurements of HC_3N, we utilize a detailed chemical model of IRC+10216.

4.1. Chemical Modeling

The chemical kinetics model used is that of Van de Sande & Millar (2022), which includes the effect of stellar companion UV photons on the gas-phase chemistry throughout the outflow. Several assumptions go into the model to reduce the complexity of the problem. The 1D model does not include dust formation and growth, but assumes dust is present from a radius R_{dust} onwards. The companion is assumed to be at the center of the outflow and to lie within the dust-free region before R_{dust}. Considering the scale of the outflow, we consider the effect of misplacing the companion within the dust-free region to be negligible. The photon flux of the companion is approximated by blackbody radiation and is set by the stellar radius, R_*, and blackbody temperature, T_{comp}. The 1D nature of the model implies that orbital motion cannot be taken into account. Hence, the companion's radiation field is assumed to be always present. This assumption is explored further in the Appendix. The model assumes the companion to be one of three types: a red dwarf at 4000 K, a solar-like star at 6000 K, or a white dwarf at 10,000 K.

The effects of a clumpy outflow on the chemistry are taken into account using the porosity formalism, as described by Van de Sande et al. (2018). The formalism divides the outflow in a stochastic two-component medium, consisting of a rarified interclump component and an overdense clumped component, and allows us to include the influence of a clumpy outflow on the penetration of UV photons along with the effect of local overdensities. Dust and gas are assumed to be well mixed in the interclump and clumped components. The specific locations of the clumps cannot be specified. Rather, the clumpiness of the outflow is determined by three general parameters: the interclump density contrast, f_{ic}, which describes the distribution of material between the clump and interclump component, the volume filling factor, f_{vol}, which sets the fraction of the total outflow volume occupied by clumps, and the size of the clumps at the stellar surface, l_*. As the volume filling factor is assumed to be constant throughout the outflow and the clumps are assumed to be mass conserving, the clumps expand as they move away from the AGB star.

The values of the three porosity parameters are observationally constrained. The shells and their clumps were resolved in the VLA survey of Keller (2017). At a distance of about $24''$ from the star, the angular sizes of the clumps were found to range from $2''0 \times 3''0$ up to $3''0 \times 7''7$. Assuming a distance of 130 pc, this corresponds to an upper limit on the physical sizes of the clumps of $3.9–15.6 \times 10^{15}$ cm at a distance of $\sim 4.6 \times 10^{16}$ cm from the star. This constrains the value of l_* to $2–4 \times 10^{13}$ cm. The density contrast between the shell and intershell region was found to lie between 1.5 and 7.6 at a radial distance of $\sim 15''$ from the star. This is consistent with the shell–intershell brightness contrast of $\geqslant 3$ retrieved by Cernicharo et al. (2015). Assuming this density contrast can be applied to the clumped and interclump components, the values of f_{ic} and f_{vol} are linked following

$$\frac{\rho_{cl}}{\rho_{ic}} = \frac{1 - (1 - f_{vol})f_{ic}}{f_{vol} f_{ic}}, \qquad (5)$$

Table 2
Physical Parameters of the Chemical Model

Parameters Adopted from Agúndez et al. (2012)	
Outflow velocity, v_∞	14.5 km s^{-1}
Stellar radius, R_*	4×10^{13} cm
Stellar temperature, T_*	2330 K
Exponent $T(r)$, ϵ	0.5
Modeling Results	
Mass-loss rate, $\dot{M}$	$1.8 \times 10^{-5}\ M_\odot$ yr^{-1}
Interclump density contrast, f_{ic}	0.50
Clump volume filling factor, f_{vol}	0.25–0.80
Companion temperature, T_{comp},	6000 K
Companion radius, R_{comp},	8.14×10^{10} cm
Onset of dust extinction, R_{dust}	$5\ R_*$
Start of the model	$1.025 \times R_{dust}$

with ρ_{cl} and ρ_{ic} the clumped and interclump densities, respectively. Lastly, we assume that dust grains are purely absorbing and therefore neglect the scattering of UV photons. Jones et al. (2013) showed that for small hydrocarbon dust grains, which provide the extinction at UV wavelengths, their albedo is essentially zero at these wavelengths. Such small grains are thought to be present in the inner envelope (Fonfria et al. 2022). Although the Jones et al. models are strictly for interstellar dust, their results are likely to hold for IRC+10216; thus, scattering can largely be ignored in the inner regions of the outflow.

The physical parameters adopted for the outflow of IRC +10216, together with those derived for our best-fit chemical model, are listed in Table 2. The parent species used are those of Agúndez et al. (2012), but with the initial abundance of C$_2$H$_2$ and HCN decreased by a factor of 2. This was done to ensure agreement with the results from Fonfria et al. (2008), who observed mid-IR vibrational lines of these molecules coming from the innermost regions of the envelope. Halving the initial C$_2$H$_2$ and HCN lies within the error of the abundances they retrieve for the region closest to the star, from the stellar photosphere up to 5.2 R_*, which is where our chemical model starts.

We find that to reproduce the increase in HC$_3$N in the inner region, both clumpiness and a companion are necessary. The increase is best reproduced assuming a solar-like companion and a dust condensation radius of 5 R_* together with an interclump density contrast $f_{ic} = 0.40$. Figure 8 shows the retrieved abundance profile along with chemical model results, for smooth and porous outflows both with and without a solar-like companion. The value of R_{dust} corresponds to the results of Fonfria et al. (2022), who found gradual dust growth up to 5 R_*. While the chemical model does not include dust growth, we find that this value of R_{dust} best reproduced the retrieved abundance profile. The values of f_{vol} and l_* do not have a large influence on the shape of the abundance profile and are constrained by the observational results of Keller (2017).

Although a mass-loss rate of $2.7 \times 10^{-5}\ M_\odot$ yr^{-1} was used for the radiative transfer model to describe the envelope density within a radius of 15″ (Guelin et al. 2018), a lower one is needed for the chemistry model since the entire extended envelope contributes to the extinction of UV photons, and lower average mass-loss rates have been obtained when
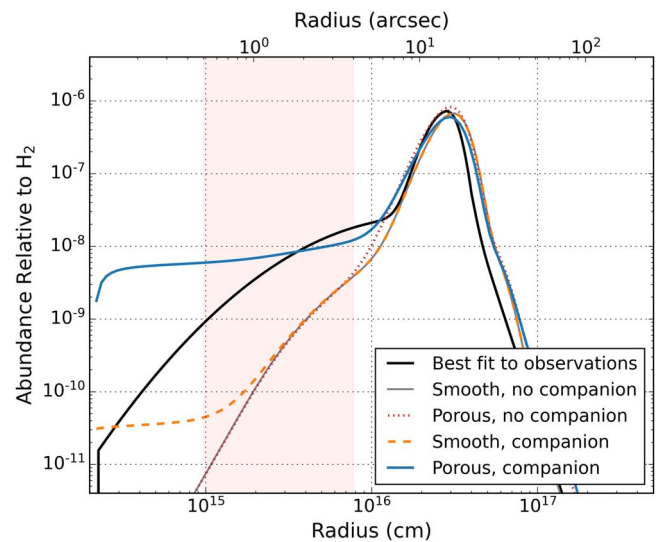
Figure 8. The retrieved HC$_3$N abundance (black) together with the chemical modeling results. Gray, solid: Smooth outflow without a stellar companion. Red, dotted: Porous outflow (characterized by $f_{ic} = 0.40$, $f_{vol} = 0.50$, and $l_* = 2 \times 10^{13}$ cm) without a stellar companion. Orange, dashed: Smooth outflow with a solar-like companion and dust condensation radius $R_{dust} = 5\ R_*$. Blue, solid: Porous outflow with a solar-like companion and $R_{dust} = 5\ R_*$. The shaded red region represents the radii where the HC$_3$N abundance is best sampled by the observations.

considering radii out to 300″ (Teyssier et al. 2006; Decin et al. 2011; Cernicharo et al. 2015). Therefore, to better fit the attenuation of the extended molecular shell, the mass-loss rate was changed from $2.7 \times 10^{-5}\ M_\odot$ yr^{-1}, as retrieved by Guelin et al. (2018), to $1.8 \times 10^{-5}\ M_\odot$ yr^{-1}.

While the porous model with a solar-like companion shows an increased HC$_3$N abundance before the molecular shell at $\sim$15″, the gentle increase in the retrieved abundance cannot be reproduced. This is because the model cannot take the gradual dust growth in the inner wind into account (Fonfria et al. 2022) and starts only after the dust condensation radius, leading to an abrupt start of photochemistry in the inner wind and subsequently a sharp increase in HC$_3$N abundance. Additionally, the porosity formalism provides only a 1D approximation of the 3D clumpy substructure seen in IRC+10216's outflow. Nevertheless, it is once again clear that a classical chemical

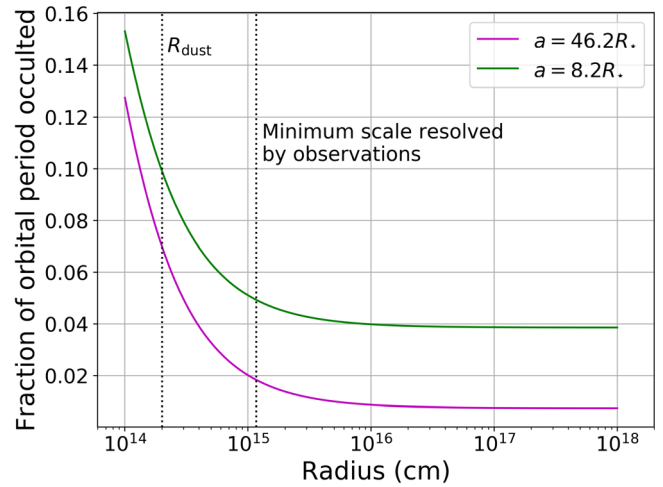model of smooth outflow without a stellar companion does not suffice.

5. Conclusions

We have presented an investigation of warm HC$_3$N emission in the inner layers of IRC+10216 utilizing multiple archival ALMA observations. Mapping the $J = 28 - 27$, $J = 30 - 29$, and $J = 38 - 37$ lines of this molecule reveals the most compact distribution ($r < 10^{16}$ cm) of a cyanopolyyne molecule presently detected toward the outflow of an evolved star, with emission localized to radii where CH$_3$CN, NaCN, H$_2$O, and C$_4$H$_2$ were previously observed (Agundez et al. 2015, 2010; Quintana-Lacaci et al. 2017; Fonfria et al. 2018). The emitting region is almost completely distinct from previous works that imaged lower-excitation lines of HC$_3$N, allowing for an in-depth characterization of this molecule throughout the CSE. Using a 1D model of the physical conditions surrounding IRC +10216, we used visibility-sampled LIME simulations to derive an average abundance of 10^{-8} with respect to H$_2$ for HC$_3$N at the radii probed by these observations. This is about five to ten times larger than predicted by simple chemical models of IRC+10216, suggesting that photochemistry is occurring more rapidly than expected in these warmer layers.

To explain this result, we investigated the possibility that the enhancement of HC$_3$N surrounding IRC+10216 is caused by an embedded binary companion emitting UV photons in the inner wind and driving photochemistry. Using known constraints on the physical environment and the abundances of parent molecules, we ran a specialized chemical kinetics network to model the radial HC$_3$N abundance profile for a variety of different companion scenarios. We find that invoking a solar-like companion and a dust condensation radius of $5\,R_*$ produces a similar abundance feature in the inner wind to that observed, and conclude that this is a strong explanation for the anomalous abundances of product molecules observed at small radii toward IRC+10216.

This result is especially intriguing when considering the newfound prevalence of binary interactions in AGB outflows (e.g., Decin et al. 2020). Since these systems appear to be common among nearby evolved stars, it could be that companions embedded in CSEs have a notable chemical affect on the composition of material returned to the ISM during the AGB and onward. In order to understand the full extent of this effect in IRC+10216, further millimeter and IR studies of photochemistry products (specifically their higher-energy transitions) will be crucial. In addition, rigorous molecular line studies of C- and O-rich evolved stars that show signs of binary shaping could shed important light on this topic.

Figure A1. Occultation time of a companion star orbiting with IRC+10216 semimajor axis a as seen by a point on the orbital plane as a function of radius. Magenta and green curves correspond to the semimajor axes proposed in Cernicharo et al. (2015) and Decin et al. (2015), respectively.

Appendix
Effect of Orbit Geometry

The orbital motion of a stellar companion could induce chemical asymmetries in the outflow. Because the chemical model is 1D, orbital motion cannot be taken into account. Moreover, the companion star is assumed to be located at the center of the AGB star, resulting in a continuous irradiation of the outflow by the companion star. Van de Sande & Millar (2022) argue that the limitations of the model are reasonable first-order approximations for a close-by companion with a short orbital period. This assumption should be investigated in more detail for the IRC+10216 system because the tentative orbital solutions presented in Cernicharo et al. (2015) and Decin et al. (2015) of, respectively, 700 and 55 yr cannot necessarily be considered sufficiently short. For a given point at radius r in the outflow on the orbital plane of the binary system, assuming a circular orbit, the fraction of the period the companion spends behind the AGB star is given by

$$f \approx \frac{2a \arctan\left[\frac{r + a}{a} \frac{R_*}{r}\right]}{2\pi a}, \quad (A1)$$

where a is the semimajor axis and R_* is the radius of the AGB star, provided $r \gg R_*$. Using the empirical values from Cernicharo et al. (2015; $a = 42.6\,R_*$) and Decin et al. (2015; $a = 8.2\,R_*$), we obtain the results shown in Figure A1. In both cases, the perceived occultation time of the companion is less than 10% of the total period at all radii larger than R_{dust}. In the

outer envelope, this value then drops to 4% and 1% for the long- and short-period solutions, respectively. From this, we would only expect time-dependent spatial chemistry differences to occur in the innermost regions of the envelope, and these scales are unfortunately not probed by our ALMA observations. Of course, other factors, including the varied dust extinction between the companion and the point as the companion orbits, the eccentricity, the presence of density enhancements, clumps, arcs, etc., do complicate the picture but as a first approximation it is clear that the companion photons are visible for a very large fraction of the orbit even in the long-period solution from Cernicharo et al. (2015).

The other important detail here is the inclination of the orbit with respect to the observer. Since we are only mapping the HC_3N distribution at the systemic velocity, we would only expect chemical asymmetries to arise in regions opposite where the companion crosses the plane of the sky, which is a small fraction even for slight inclinations. Though the exact orbit is uncertain, Decin et al. (2015) proposed that the inclination is larger than 60° based on observed ^{13}CO position–velocity diagrams. An inclination this high would only cause chemical asymmetries (in the plane of the sky) to be observable if the envelope was observed during very specific points in the orbit, which is unlikely given the proposed period of 55–700 yr (Cernicharo et al. 2015; Decin et al. 2015). Between this and the relatively short fractional occultation period, if a companion is indeed influencing HC_3N chemistry in the envelope of IRC +10216, we do not expect orbit-induced asymmetries to be prominent or detectable in the ALMA images presented in this work.

ORCID iDs

Mark A. Siebert ⓘ https://orcid.org/0000-0002-8505-4934
Marie Van de Sande ⓘ https://orcid.org/0000-0001-9298-6265
Thomas J. Millar ⓘ https://orcid.org/0000-0001-5178-3656
Anthony J. Remijan ⓘ https://orcid.org/0000-0001-9479-9287

References

Agundez, M., Cernicharo, J., & Guelin, M. 2010, ApJL, 724, L133
Agundez, M., Cernicharo, J., Quintana-Lacaci, G., et al. 2015, ApJ, 814, 143
Agúndez, M., Cernicharo, J., Quintana-Lacaci, G., et al. 2017, A&A, 601, A4
Agúndez, M., Fonfría, J. P., Cernicharo, J., et al. 2012, A&A, 543, A48
Agundez, M., Fonfria, J. P., Cernicharo, J., Pardo, J. R., & Guelin, M. 2008, A&A, 479, 493
Agúndez, M., Martínez, J. I., de Andres, P. L., Cernicharo, J., & Martín-Gago, J. A. 2020, A&A, 637, A59
Brinch, C., & Hogerheijde, M. R. 2010, A&A, 523, A25
Brunner, M., Danilovich, T., Ramstedt, S., et al. 2018, A&A, 617, A23
Cernicharo, J., Guelin, M., & Kahane, C. 2000, A&AS, 142, 181
Cernicharo, J., Marcelino, N., Agúndez, M., & Guélin, M. 2015, A&A, 575, A91
Cernicharo, J., Teyssier, D., Quintana-Lacaci, G., et al. 2014, ApJL, 796, L21
Cherchneff, I. 2012, A&A, 545, A12
Cornwell, T. J. 2008, ISTSP, 2, 793
Cortes, P. C., Remijan, A., Biggs, A., et al. 2020, ALMA Technical Handbook, ALMADoc. 8.4, ver. 1.0 , ISBN 978-3-923524-66-2 https://almascience.eso.org/documents-and-tools/cycle8/alma-technical-handbook
Costagliola, F., & Aalto, S. 2010, A&A, 515, A71
De Beck, E., Lombaert, R., Agundez, M., et al. 2012, A&A, 539, A108
Decin, L. 2021, ARA&A, 59, 337
Decin, L., Montarges, M., Richards, A. M. S., et al. 2020, Sci, 369, 1497
Decin, L., Richards, A. M. S., Danilovich, T., Homan, W., & Nuth, J. A. 2018, A&A, 615, A28

Decin, L., Richards, A. M. S., Neufeld, D., et al. 2015, A&A, 574, A5
Decin, L., Royer, P., Cox, N. L. J., et al. 2011, A&A, 534, A1
Deguchi, S., & Uyemura, M. 1984, ApJ, 285, 153
Dinh-V-Trung, & Lim, J. 2008, ApJ, 678, 303
Faure, A., Lique, F., & Wiesenfeld, L. 2016, MNRAS, 460, 2103
Fonfria, J. P., Agundez, M., Cernicharo, J., Richter, M. J., & Lacy, J. H. 2018, ApJ, 852, 80
Fonfria, J. P., Cernicharo, J., Richter, M. J., & Lacy, J. H. 2008, ApJ, 673, 445
Fonfria, J. P., DeWitt, C. N., Montiel, E. J., Cernicharo, J., & Richter, M. J. 2022, ApJL, 927, L33
Gordon, I. E., Rothman, L. S., Hargreaves, R. J., et al. 2022, JQSRT, 277, 107949
Guelin, M., Lucas, R., & Cernicharo, J. 1993, A&A, 280, L19
Guelin, M., Patel, N. A., Bremer, M., et al. 2018, A&A, 610, A4
He, J. H., Dinh-V-Trung, Hasegawa, T. I., et al. 2017, ApJ, 845, 38
He, J. H., Dinh-V-Trung, Kwok, S., et al. 2008, ApJS, 177, 275
He, J. H., Kaminski, T., Mennickent, R. E., et al. 2019, ApJ, 883, 165
Homan, W., Danilovich, T., Decin, L., et al. 2018, A&A, 614, A113
Homan, W., Montargès, M., Pimpanuwat, B., et al. 2020, A&A, 644, A61
Jolly, A., Benilan, Y., & Fayt, A. 2007, JMoSp, 242, 46
Jones, A. P., Fanciullo, L., Kohler, M., et al. 2013, A&A, 558, A62
Keady, J. J., & Ridgway, S. T. 1993, ApJ, 406, 199
Keller, D. 2017, PhD thesis, Max Planck Institute for Radio Astronomy, Bonn, Germany
Kervella, P., Montarges, M., Ridgway, S. T., et al. 2014, A&A, 564, A88
Khouri, T., Vlemmings, W. H. T., Ramstedt, S., et al. 2016, MNRAS, 463, L74
Kim, H., Lee, H.-G., Mauron, N., & Chu, Y.-H. 2015a, ApJL, 804, L10
Kim, H., Lee, H.-G., Ohyama, Y., et al. 2021, ApJ, 914, 35
Kim, H., Liu, S.-Y., Hirano, N., et al. 2015b, ApJ, 814, 61
Knapp, G. R., & Chang, K. M. 1985, ApJ, 293, 281
Lagadec, E., Verhoelst, T., Mekarnia, D., et al. 2011, MNRAS, 417, 32
Leao, I. C., de Laverny, P., Mekarnia, D., De Medeiros, J. R., & Vandame, B. 2006, A&A, 455, 187
Li, X., Millar, T. J., Heays, A. N., et al. 2016, A&A, 588, A4
Loomis, R. A., Oberg, K. I., Andrews, S. M., et al. 2018, AJ, 155, 182
Maercker, M., Vlemmings, W. H. T., Brunner, M., et al. 2016, A&A, 586, A5
Massalkhi, S., Agundez, M., & Cernicharo, J. 2019, A&A, 628, A62
Mauron, N., & Huggins, P. J. 2006, A&A, 452, 257
McGuire, B. A. 2022, ApJS, 259, 30
McMullin, J. P., Waters, B., Schiebel, D., Young, W., & Golap, K. 2007, in ASP Conf. Ser. 376, Astronomical Data Analysis Software and Systems XVI, ed. R. A. Shaw, F. Hill, & D. J. Bell (San Francisco, CA: ASP), 127
Men'shchikov, A. B., Balega, Y., Blocker, T., Osterbart, R., & Weigelt, G. 2001, A&A, 368, 497
Millar, T. J. 2020, ChJCP, 33, 668
Muller, H. S. P., Schloder, F., Stutzki, J., & Winnewisser, G. 2005, JMoSt, 742, 215
Ossenkopf, V., & Henning, T. 1994, A&A, 291, 943
Pardo, J. R., Cernicharo, J., Velilla Prieto, L., et al. 2018, A&A, 615, L4
Petrie, S. 1996, MNRAS, 282, 807
Quintana-Lacaci, G., Cernicharo, J., Velilla Prieto, L., et al. 2017, A&A, 607, L5
Ramstedt, S., Mohamed, S., Vlemmings, W. H. T., et al. 2017, A&A, 605, A126
Sahai, R., Huang, P.-S., Scibelli, S., et al. 2022, ApJ, 929, 59
Sahai, R., Lee, C.-F., Contreras, C. S., et al. 2017, ApJ, 850, 158
Sahai, R., Morris, M., Sanchez Contreras, C., & Claussen, M. 2007, AJ, 134, 2200
Santoro, G., Martinez, L., Lauwaet, K., et al. 2020, ApJ, 895, 97
Tenenbaum, E. D., Dodd, J. L., Milam, S. N., Woolf, N. J., & Ziurys, L. M. 2010, ApJS, 190, 348
Teyssier, D., Hernandez, R., Bujarrabal, V., Yoshida, H., & Phillips, T. G. 2006, A&A, 450, 167
Van de Sande, M., & Millar, T. J. 2022, MNRAS, 510, 1204
Van de Sande, M., Sundqvist, J. O., Millar, T. J., et al. 2018, A&A, 616, A106
van der Tak, F., Lique, F., Faure, A., Black, J., & van Dishoeck, E. 2020, Atoms, 8, 15
van der Tak, F. F. S., Black, J. H., Schoier, F. L., Jansen, D. J., & van Dishoeck, E. F. 2007, A&A, 468, 627
Weiss, A., & Ferguson, J. W. 2009, A&A, 508, 1343
Winters, J. M., Fleischer, A. J., Gauger, A., & Sedlmayr, E. 1994, A&A, 290, 623
Ziurys, L. M. 2006, PNAS, 103, 12274